



Three-dimensionality of slab detachment due to ridge-trench collision: Laterally simultaneous boudinage versus tear propagation

Erin R. Burkett and Magali I. Billen

*Department of Geology, University of California, 1 Shields Avenue, Davis, California 95616, USA
(erburkett@ucdavis.edu; mibillen@ucdavis.edu)*

[1] The detachment of subducted tectonic plates is a process that has been increasingly associated with collisional scenarios and the end of subduction in various locations worldwide. In particular, the propagation of slab detachment (“tearing”) of a subducting plate has been described in conceptual models as a cause for spatially and temporally progressing surface effects such as slab gap volcanism and uplift. However, there is little understanding of the causes and dynamics associated with three-dimensional (3-D) slab tearing, especially in the case of ridge-trench collision. Here we show using fully dynamic 3-D numerical models that the process of detachment due to ridge-trench collision depends on the geometry of the ridge segments approaching the trench. For a finite laterally symmetric slab, the 3-D detachment process occurs nearly simultaneously along strike by way of boudinage-type necking and opening of holes central to the slab. For a case involving the approach of two offset ridge segments to the trench, slab tearing occurs in the form of (1) a vertical propagating separation along the age offset boundary within the slab that was previously weakened by a transform weak zone and (2) horizontal propagating detachment controlled by lateral transfer of slab pull to adjacent surface plate segments. However, lateral decoupling between offset adjacent plate segments and the propagating nature of the vertical and horizontal tearing are dependent upon fracture zones remaining weak through the subduction zone. Whether detachment occurs simultaneously along strike or propagates laterally, the process is controlled by plastic yielding of the slab interior when young lithosphere entering the trench can no longer support slab pull.

Components: 11,900 words, 11 figures, 2 tables.

Keywords: detachment; break-off; ridge-trench collision; subduction.

Index Terms: 8170 Tectonophysics: Subduction zone processes (1031, 3060, 3613, 8413); 8120 Tectonophysics: Dynamics of lithosphere and mantle: general (1213); 4255 Oceanography: General: Numerical modeling (0545, 0560, 1952).

Received 2 July 2010; **Revised** 16 September 2010; **Accepted** 21 September 2010; **Published** 24 November 2010.

Burkett, E. R., and M. I. Billen (2010), Three-dimensionality of slab detachment due to ridge-trench collision: Laterally simultaneous boudinage versus tear propagation, *Geochem. Geophys. Geosyst.*, 11, Q11012, doi:10.1029/2010GC003286.

1. Introduction

[2] Recognition and understanding of the tearing and detachment of subducted portions of lithosphere (slabs) has major implications for the causes of changes in tectonic plate motions, coupling across

plate boundaries, mantle flow patterns through slab gaps and around slab edges, and timing of surface effects such as slab gap volcanism, topography, and regional stress. The process of ridge-trench collision in particular is a process that may lead to slab detachment and cessation of subduction due to the



combined effects of greater buoyant resistance of young lithosphere to subduction and a decrease in plate strength with proximity to the ridge axis.

[3] Along the western North American plate margin, for instance, the loss of most of the Farallon plate upon ridge-trench collision has led to a reorganization of relative plate motion directions that has caused transitions in magmatism and stress regimes along the boundary [Dickinson, 1997; Atwater and Stock, 1998]. Progressive cessation of subduction with the approach of the East Pacific Rise (EPR) seems to have resulted at least in part from the detachment of the Farallon plate as evidenced by abandonment of ridge segments (e.g., outboard of Baja California [Mammerickx and Klitgord, 1982; Lonsdale, 1991]). Ferrari [2004] also suggests a related southeastward propagating tear responsible for a pulse of non-subduction-related arc volcanism within the Trans-Mexican Volcanic Belt (TMVB). Globally, many sites of similar slab window volcanism have been attributed to “ridge subduction” in which the ridge axis itself has been subducted and opens a slab window shallow enough to induce melting and cause volcanism including both a slab and mantle signature [Thorkelson, 1996; Iwamori, 2000]. However, observations of ridge abandonment (e.g., Baja California [Pallares *et al.*, 2007]), positioning of magmatism with respect to projected ridge axis subduction (e.g., Chile [Guivel *et al.*, 2006]), and two-dimensional (2-D) numerical models of ridge-trench collision [Burkett and Billen, 2009] suggest instead that in some cases slab detachment may occur before a ridge can be subducted.

[4] In previous 2-D numerical modeling studies, slab detachment is characterized by necking of a subducted slab as controlled by plastic yielding [Andrews and Billen, 2009] or thermal weakening [Gerya *et al.*, 2004; Andrews and Billen, 2009], with the former mechanism tending to involve quicker and shallower detachment than the latter. Other mechanisms that may control or facilitate detachment and affect detachment timing and depth include increased negative buoyancy associated with the olivine-spinel phase transition [Zlotnik *et al.*, 2008; Baumann *et al.*, 2010], Peierls creep [Duretz *et al.*, 2010], and shear heating [Gerya *et al.*, 2004], which we do not incorporate in the models presented here for the sake of providing preliminary constraints on first-order rheologic controls. Decreasing age of the subducted slab during ridge-trench approach, as studied here, combines a thermal control with a plastic yielding control on detachment since the integrated slab

strength to overcome for break-off to occur depends on both the maximum yield strength and the slab age (or thickness), as demonstrated in 2-D numerical models by Burkett and Billen [2009]. An understanding of the 2-D detachment dynamics provides a necessary basis for separating 2-D rheologic controls from 3-D geometric effects. In the 3-D models presented here, for instance, lateral differences in slab thermal structure, such as warmer slab temperatures near slab edges, can lead to variations along strike in the mechanisms controlling detachment (e.g., yielding of the slab center and more thermally controlled detachment at the edges).

[5] Current conceptual models of the nature of 3-D slab detachment largely focus on horizontal propagation of slab detachment, particularly originating at a slab edge and propagating laterally due to the concentration of slab pull at the tip of the tear within the slab [Yoshioka and Wortel, 1995], but such studies depend upon the initial assumption of the existence of a tear initiating at the edge and do not explore the process before the initiation of tearing. Rosenbaum *et al.* [2008] outline five conceptual models of types of slab tearing: final/complete detachment of a slab along strike (without specifying the detailed detachment process preceding), vertical tear propagation (illustrated as upward propagating), horizontal tear propagation, tear fault propagation (at the surface) separating two subducting segments, and tear faults propagating on either side of a slab rolling back faster than adjacent slabs. Results of the 3-D detachment models presented here provide more detailed and previously unrecognized views of the detachment and slab tearing process. Most importantly they identify the causes of different modes of slab detachment, including previously unrecognized modes such as vertical downward tearing along a thermally offset and transform-weakened boundary between slab segments, and the opening of slab gaps central to the slab rather than originating at a slab edge.

2. Modeling Methods

[6] This study builds upon previous 2-D modeling of ridge-trench collision [Burkett and Billen, 2009] by including ridge segments and a subduction zone that have a finite length in the latitudinal direction, with the 2-D cross section in depth and longitude representing a trench-perpendicular slice of a subduction zone in which a ridge approaches perpendicular to the trench (see section 2.2). The models allow subduction to occur dynamically due to slab pull and ridge push. A weakened shear zone



decouples the subducting plate from the overriding plate to allow subduction to occur, and similarly weakened transform weak zones free the subducting plate laterally from the surrounding plate to allow the subducting plate to respond to slab pull. While the 2-D models are a necessary step in isolating first-order 2-D controls on the detachment process, the 3-D models presented here more closely approach conditions within the Earth and are necessary to test uniquely 3-D effects such as lateral flow variations and tear propagation.

2.1. Numerical Method

[7] We use **CitcomCU**, a 3D finite element code that solves thermal convection problems in spherical geometry and allows for the use of complex boundary conditions, large variations in rheologic parameters, and localized mesh refinement [Moresi *et al.*, 1996; Zhong, 2006]. We solve the standard equations for conservation of mass, momentum, and energy for thermal convection without internal heating and assuming incompressible flow and the Boussinesq approximation,

$$\nabla \cdot \mathbf{u} = 0 \quad (1)$$

$$\nabla \cdot \boldsymbol{\sigma} + \mathbf{f} = 0 \quad (2)$$

$$\dot{T} = -\mathbf{u} \cdot \nabla T + \kappa \nabla^2 T \quad (3)$$

where \mathbf{u} is the velocity, $\mathbf{f} = \rho_o \alpha (T - T_o) g \delta_{rr}$ is the force due to density variations related to temperature ($\rho_o = 3300 \text{ kg/m}^3$ is density, $\alpha = 2.0 \times 10^{-5} \text{ K}^{-1}$ is the coefficient of thermal expansion, $T_o = 1400^\circ\text{C}$ is the reference mantle temperature, and $g = 9.8 \text{ m/s}^2$ is gravitational acceleration, and δ_{rr} is the Dirac delta function), and $\sigma_{ij} = -P\delta_{ij} + \eta\dot{\epsilon}_{ij}$, where η is viscosity and $\dot{\epsilon}_{ij} = \frac{1}{2} \left[\frac{\partial u_i}{\partial x_j} + \frac{\partial u_j}{\partial x_i} \right]$ is the stress tensor defining the constitutive relation. The total pressure, P , includes the lithostatic pressure (without compressibility) and the dynamic pressure resulting from viscous flow (e.g., $P = P_{\text{lithostatic}} + P_{\text{dynamic}}$). Instantaneous dynamic topography is calculated as $h = \sigma_{rr}/\rho_o g$ from surface normal stresses at the top of the model domain.

2.2. Model Setup

[8] The full model domain (Figure 1a) is a 3-D portion of a sphere that extends 1350 km in depth (from the surface), 29° in longitude ($\sim 3220 \text{ km}$ at the surface), and 26° in latitude ($\sim 2890 \text{ km}$ at the surface). The initial temperature structure includes an overriding plate of constant thermal thickness

(corresponding to an initial age of 60 Myr) surrounding a partially subducted 300 km wide plate with a slab reaching 600 km depth (Figure 1b). The subducted plate in model 3d1 (Figure 1c, top) contains a single trench-parallel ridge initially located 300 km outboard of the trench, whereas models 3d2 and 3d3 (Figure 1c, bottom) contain two ridge segments located 300 and 450 km outboard of the trench, each 150 km wide (in latitude) and offset by 150 km. We refer to the northern plate segment as plate A and the southern segment as plate B, and we refer to their respective subducted slabs as slab A and slab B. The thermal structure of the subducting plate is initially determined according to the half-space cooling model by increasing thickness with distance from the ridge based on a spreading rate of 2.5 cm/yr. The initial subducted slab shape and minimum slab temperature with depth are based on slab profiles generated in dynamic models by Billen and Hirth [2007]. The choice of an initial slab depth of 600 km is based on 2-D results [Burkett and Billen, 2009] showing this length is sufficient to represent any slab long enough to be supported by a higher-viscosity lower mantle. The behavior of a shorter slab includes faster sinking within the upper mantle followed by a readjustment in the speed of dynamics upon interaction with the lower mantle, which are effects that need not be explored again in this study.

[9] The mesh element size varies in longitude from 2.8 km in a 1000 km wide section centered on the subduction zone to 14 km at the sides of the model domain. The longitudinal resolution is also higher (1.4 km) in a 60 km wide region including the mantle wedge. In latitude, the elements are 5 km wide for a region encompassing the entire subducting plate and transform weak zones and increases to a maximum of 15 km at the sides of the domain. In depth, the element height increases from 1.5 km in the top 300 km of the mesh to a maximum of 10 km in the lower mantle. All boundaries are free slip. Temperatures are fixed at the top and bottom boundaries and range from 0°C (surface) to 1400°C (maximum nonadiabatic mantle temperature). No velocities are imposed on the subducting or overriding plate.

[10] The 3-D model setup is nearly an exact extension in the latitudinal direction of our previous 2-D models [Burkett and Billen, 2009], with the exception of a reduction of the longitude-depth domain size to optimize the design of the 3-D models for better convergence and quicker run time. The domain depth in the models presented here is

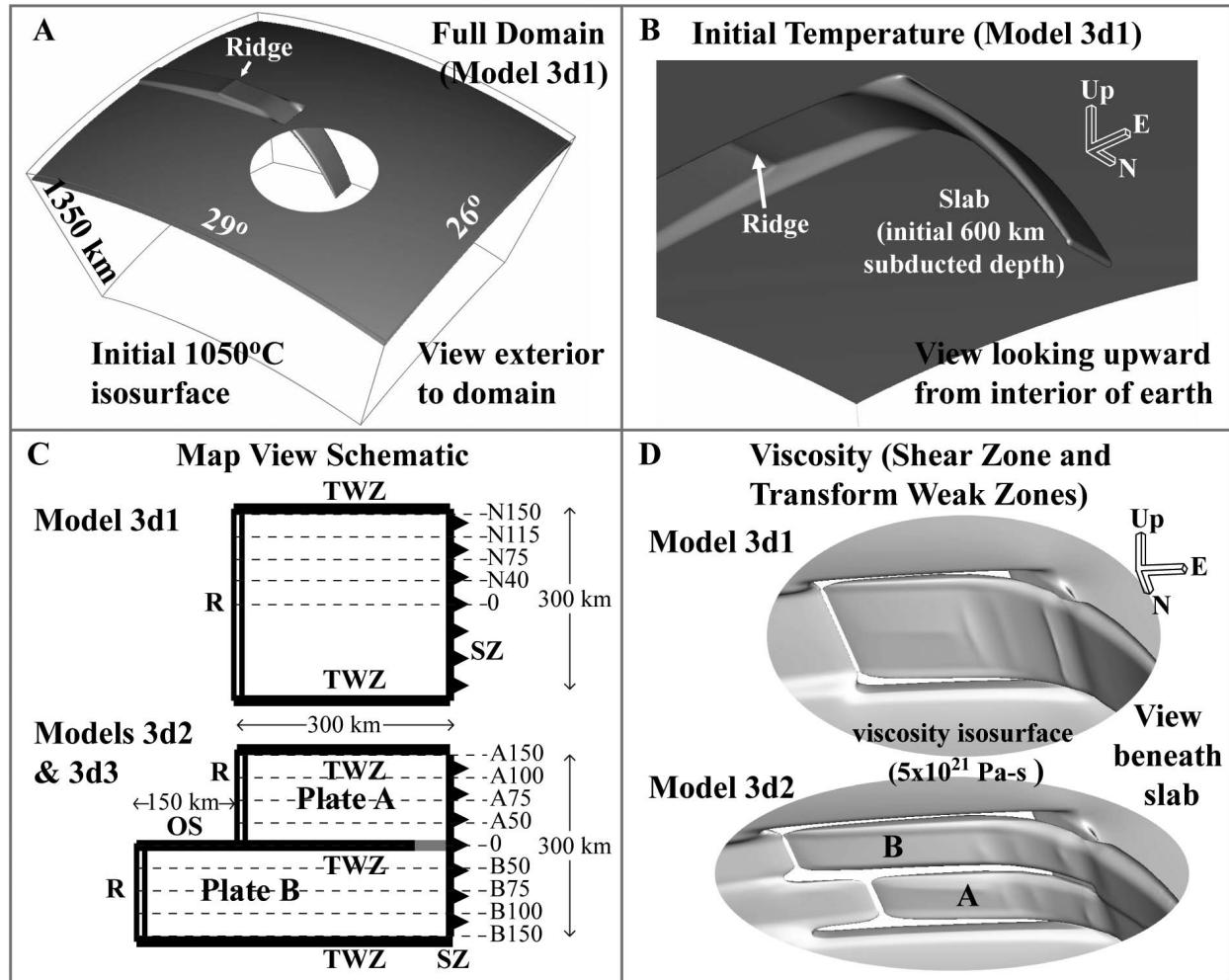


Figure 1. Model domain and initial temperature and weak region setup. (a) Temperature isosurface (1050°C) for model 3d1 full domain shown from above, including a cutout to see the subducted slab. (b) Initial temperature isosurface for model 3d1 showing slab and ridge thermal structure for a view looking upward from within the Earth (the same viewpoint used for subsequent presentation of model results in Figures 3 and 9). (c) Map view schematics of setup for models 3d1, 3d2, and 3d3 (SZ, shear zone or subduction zone; R, ridge; TWZ, transform weak zone; OS, offset between ridges). Dashed lines indicate latitudes at which results for trench-perpendicular cross sections of the 3-D slabs are presented in Table 2. Latitude labels indicate distance in km from the central latitude; “N” refers to northern latitudes for model 3d1, and “A” and “B” indicate cross sections of plate/slab A and plate/slab B, respectively, for models 3d2 and 3d3. The difference between models 3d2 and 3d3 is indicated by the gray portion of the central transform weak zone, which extends to the shear zone in model 3d2 but ends (“heals”) 50 km outboard of the trench in model 3d3. (d) Views looking upward from beneath viscosity isosurfaces ($5 \times 10^{21} \text{ Pa s}$) for (top) model 3d1 and (bottom) model 3d2, showing the effects of the ridges, shear zone, and transform weak zones on freeing the subducting plates from the surrounding plate.

shortened by 1540 km and longitudinal width shortened by 14° (10° of which is cut from the west to minimize return flow effects on dynamics). Despite the noted quickening of dynamics caused by a reduction of domain size in previous 2-D model results [Burkett and Billen, 2009], the effect here of also limiting the minimum viscosity (the only other difference from previous models, see section 2.4)

dominates over any effects of changing the domain size. This is because the viscosity limit slows the dynamics and minimizes the effect of return flow, which might otherwise be amplified by a decrease in domain size.

[11] To provide a direct 2-D to 3-D comparison, we include here the results of two 2-D models

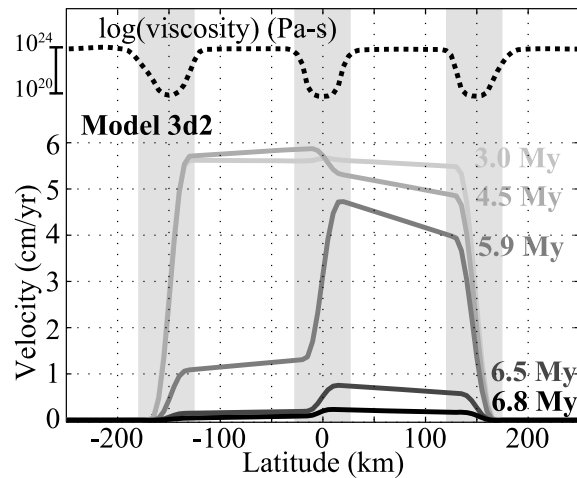


Figure 2. Latitude profiles of subducting plate velocity at four times for model 3d2. Solid lines are profiles of the trench-perpendicular component of the plate subduction velocity at a longitude 50 km outboard of the trench. Vertical shaded regions indicate the latitudinal positioning of the transform weak regions, encompassing the total width of smoothing from the maximum central weakening to the background viscosity. A profile of the log of viscosity at the surface (dotted line) shows the viscosity range across the transform weak zones from 10^{20} Pa s at the center to a maximum of 10^{24} Pa s for the unweakened surface plate.

(model 2dA and model 2dB) equivalent to the central latitude cross sections of the ridge segments in the 3-D models (model 3d1 and model 3d2). These 2-D models include the same longitude-depth domain size as the 3-D models. Model 2dA is the same as the previous 2-D reference model except for the viscosity lower limit and domain change.

2.3. Weak Regions: Shear Zone and Transform Weak Zones

[12] In order for subduction to occur within the models, the inclusion of fixed zones of prescribed weakened viscosity allows decoupling of the subducting plate from the surrounding overriding plate and represent the subduction shear zone and transform faults or fracture zones. Although the zones would ideally be represented by faults of narrow width, the closest approximation to fault behavior in these models is the presence of a sufficiently narrow zone of weakened viscosity. The nonlinear rheology is particularly effective in allowing localization of strain rates in such weak regions to better represent narrow boundaries between rigid plates. The weak regions within the 3-D models presented here

consist of two types: (1) a shear zone 30 km wide (perpendicular from the slab surface) that separates the top of the subducting plate from the overriding plate to a depth of 110 km and extends uniformly in latitude along the subduction zone and (2) transform weak zones 110 km deep, 60 km wide in latitude, and extending in longitude from the farthest ridge to the shear zone.

[13] The weakening is prescribed as a maximum viscosity such that viscosities may dynamically evolve to be lower within the weak region as a result of the stress- and temperature-dependent rheology, but cannot become greater than the prescribed value. The zones are smoothed toward the background viscosity such that the center of a weak zone prescribes the maximum weakening value (10^{20} Pa s). Viscosity isosurfaces for model 3d1 and model 3d2 illustrate the decoupling of the subducting plate and slab from the surrounding overriding plate by the shear zone and transform weak zones (Figure 1d). The central transform weak zone in model 3d2 separates plate A and plate B and allows them to move independently. A profile of viscosity along latitude shows the smooth weakening of viscosity across the transform weak zones (Figure 2). Although the vertical shaded areas show the total width of the weak zones including the smoothing, the effective width of the zones is closer to half that width (30 km) based on the accommodation of jumps in velocity within a narrower zone where the weakening leads to viscosities between 10^{21} – 10^{22} Pa s (Figure 2).

[14] The central transform weak zone in model 3d2 separating the two plate segments extends in longitude from the farthest ridge to the subduction shear zone. Ideally, the fully weakened transform weak zone would extend in longitude only between the two ridges, and a lesser weakening would represent the fracture zone portion of the boundary. However, since the weak regions prescribed in these models are fixed (in an Eulerian frame of reference) and cannot track the dynamic changes in ridge position, and in order to allow the ridge segments to migrate independently toward the subduction zone, the same weakening is needed here to represent both transform faults and fracture zones. To test the effect of the longitudinal extent of the central transform weak zone separating the plate segments, we include results for model 3d3, in which the central transform weak zone ends (“heals”) 50 km outboard of the trench (see Figure 1c), rather than separating the plates through the subduction zone as in model 3d2.



Table 1. Viscous Flow Law Parameters for Wet Olivine at Constant Water Content From *Hirth and Kohlstedt* [2003]

Flow Law Parameters			
	Parameter	Diffusion	Dislocation
n	Stress exponent	1.0	3.5
A	Preexponential factor ($\text{s}^{-1} \text{Pa}^{-n} \mu\text{m}^p C_{OH}^r$)	1.0	9.0×10^{-20}
E	Activation energy (kJ/mol)	335	480
V	Activation volume (m^3/mol)		
	Upper mantle	4.0×10^{-6}	11×10^{-6}
	Lower mantle	1.5×10^{-6}	—
d	Grain size (μm)		
	Upper mantle	10,000	—
	Lower mantle	40,000	—
p	Grain size exponent	3.0	—
C_{OH}	OH concentration (ppm H/Si)	1000	1000
r	C_{OH} exponent	1.0	1.2

2.4. Rheology

[15] The rheology of the lithosphere and mantle controls deformation interior to the Earth as well as the timing, magnitudes, and spatial variations of related observable surface effects. For instance, the choice of viscosity structure is important for the decoupling of plates, dynamic topography, viscous support of the slab, viscous resistance to subduction, and overall timing of processes. A plastic rheology plays a major role in determining slab stiffness and therefore controls the point at which slab pull overcomes the resisting forces and leads to detachment. The rheology in the models presented here consists of a composite upper mantle viscosity (deformation of olivine accommodated by both diffusion and dislocation creep), a Newtonian-only lower mantle viscosity (deformation of olivine accommodated by diffusion creep only), and a plastic rheology that limits the maximum viscosity when stress exceeds the maximum yield strength. Laboratory experiments indicate that deformation of olivine occurs by both diffusion (df) and dislocation (ds) creep in the upper mantle [*Hirth and Kohlstedt*, 2003], where each mechanism accommodates a portion of the total strain rate,

$$\dot{\epsilon} = \dot{\epsilon}_{df} + \dot{\epsilon}_{ds}. \quad (4)$$

[16] The composite upper mantle viscosity for deformation at constant stress is given by,

$$\eta_{comp} = \frac{\eta_{df}\eta_{ds}}{\eta_{df} + \eta_{ds}} \quad (5)$$

where η_{df} and η_{ds} are the diffusion creep and dislocation creep viscosities for olivine. Note that for

Newtonian-only rheology, the equation simplifies to $\eta_{comp} = \eta_{df}$. The general form of the viscosity law assuming constant stress is,

$$\eta_{df,ds} = \left(\frac{d^p}{AC_{OH}^r} \right)^{\frac{1}{n}} \dot{\epsilon}_E^{\frac{1-n}{n}} \exp \left[\frac{E + P_{lc}V}{nRT} \right] \quad (6)$$

where $\dot{\epsilon}_E = (\frac{1}{2}\dot{\epsilon}_{ij}\dot{\epsilon}_{ij})^{1/2}$ is the effective strain rate given by the square root of the second invariant of the strain rate tensor for incompressible flow [*Ranalli*, 1995], P_{lc} is the lithostatic pressure defined by a compressibility gradient in the mantle ($P_{lc} = -\frac{1}{\beta_a}\ln(1 - \rho_0 g \beta_a z)$, where z is depth and the adiabatic compressibility $\beta_a = 4.3 \times 10^{-12} \text{Pa}^{-1}$ [*Turcotte and Schubert*, 2002]), T is the temperature including the adiabatic temperature gradient ($3 \times 10^{-4} \text{K/m}$), and the parameters for diffusion and dislocation creep of olivine are given in Table 1. The flow law parameters give a background viscosity of $\eta = 10^{20} \text{Pa s}$ at a depth of 250 km and transition strain rate of $\dot{\epsilon}_t = 10^{-15} \text{s}^{-1}$ (i.e., $\dot{\epsilon}_{df} = \dot{\epsilon}_{ds}$) in agreement with estimates of upper mantle viscosity from postglacial rebound and plate velocity models [*Hager*, 1991]. The water content and grain size are chosen to fix the absolute magnitude of viscosity and the transition strain rate. CitcomCU has been modified to include a composite viscosity as in the work by *Billen and Hirth* [2007]. The composite upper mantle viscosity is approximately ten times smaller than the Newtonian lower mantle viscosity at a strain rate of $1 \times 10^{-15} \text{s}^{-1}$. Although we include an increase in viscosity between the upper and lower mantle, we do not model density effects of the 410 and 660 km phase transitions.

[17] Maximum slab stiffness, as calculated assuming a composite rheology, is greater than 1 GPa even at temperatures approaching 800°C and is much greater at colder temperatures toward shallower depths. We therefore limit the maximum stress and viscosity by also using a plastic rheology, prescribed when stress exceeds the yield strength (σ_y) such that the effective viscosity is calculated as,

$$\eta_{ef} = \min \left(\frac{\sigma_y}{\dot{\epsilon}_E}, \eta_{comp} \right) \quad (7)$$

where the depth-dependent yield strength is given by $\sigma_y = 15z + 0.1$ (σ_y in MPa and depth, z , in km) for $\sigma_y < \sigma_{y_{max}}$ and $\sigma_y = \sigma_{y_{max}}$ for $\sigma_y \geq \sigma_{y_{max}}$, and where $\dot{\epsilon}_E$ is the effective strain rate. The slope of the yield criterion corresponds to a coefficient of friction $\mu = 0.6$ and a pore fluid factor $\lambda = 0.3$ (where $\lambda = P_{fluid}/P_{lithostatic}$ for hydrostatic pore pressure [*Zoback and Townend*, 2001]), and the maximum value

($\sigma_{y_{\max}} = 500$ MPa) is reached at about 33 km depth. Previous results [Andrews and Billen, 2009; Burkett and Billen, 2009] show that within a realistic range of 300 to 1000 MPa, the effect of yield strength is understood to predictably affect the timing of detachment and is not expected to drastically change the dynamics enough to require further variations in maximum yield strength values for the 3-D models.

[18] The rheology incorporated in the models presented here is identical to that in 2-D models [Burkett and Billen, 2009] with the exception of the inclusion of a limit on the minimum allowable viscosity within the models to 1×10^{19} Pa s (there was no lower limit in the previous models; viscosities ranged as low as 2×10^{17} Pa s). Based on a rerun of the 2-D reference model from previous results with the added limitation on the minimum viscosity, the effect is a minor slowing of the dynamics (slower average subduction velocity from 9.3 to 7.5 cm/yr and time to detachment delayed to 5.3 compared to 3.9 Myr), although the general dynamics, including the rapid period of detachment within ~ 1 Myr, are otherwise the same.

[19] In the previous 2-D results [Burkett and Billen, 2009], the point of detachment was defined as the point of separation of the 1200°C temperature contour. We have decided for the 3-D models to instead use the 1050°C contour to define the point of detachment in order to minimize a distracting effect caused by the presence of Rayleigh-Taylor instabilities. The instabilities are present in both the 2-D and 3-D models and are interesting in themselves, demonstrating flow driven by the sinking slab that helps pull material from beneath the overriding plate, as delineated by the deflection of temperature contours most pronouncedly above $\sim 1100^\circ\text{C}$. Temperature deflection by instabilities varies along latitude in the 3-D models (e.g., most pronounced at the central latitude in model 3d1; Figure 6f), and therefore the choice instead of the 1050°C contour focuses more specifically on the internal slab deformation (e.g., changes in slab thickness by the necking process) associated with the detachment process rather than superimposed effects from contour deflections by instabilities.

[20] Differences in reported detachment values between choosing the 1050°C contour versus 1200°C contour are very slight. Compared to previous results reported using the 1200°C contour, the detachment point is reported here as no more than 5 km shall-

lower, 6 km more westward, and the earliest complete separation of the surface plate contour from the subducted slab contour is no more than 0.1 Myr sooner on average.

3. Results

[21] The 3-D models presented here test the modes of detachment that arise within 3-D scenarios, whether uniquely 3-D or dependent upon the 2-D controls explored in previous results [Burkett and Billen, 2009]. Table 2 presents a summary of five model results: three 3-D models, and two 2-D models corresponding to cross sections in latitude of the ridge segments in the 3-D models. In order to show the latitudinal variations in results for the 3-D models, Table 2 lists results for 3-D models at a number of positions in latitude that correspond to the trench-perpendicular cross sections (Figure 1c).

[22] Model 3d1 is designed to examine along-strike variations in the dynamics of ridge-trench collision for laterally finite parallel ridge-trench collision. Model 2dA is also presented for comparison as the 2-D equivalent of the central latitude cross section in model 3d1. Model 3d2 breaks the symmetry of subduction and ridge-trench collision by the inclusion of two offset ridge segments in order to determine the dynamics for a case in which there is a significant lateral difference in thermal structure of the subducting plate. Model 2dA can also be considered as the 2-D equivalent cross section of ridge segment A, and model 2dB is presented for 2-D comparison with ridge segment B. Model 3d3 is identical to model 3d2 with the exception that the fully weakened central transform weak zone separating plates A and B extends only to 50 km outboard of the trench. Model 3d3 is therefore designed to test the effects of variations in coupling across transform faults or fractures zones within the subduction zone on the subduction and detachment dynamics.

[23] In general, as within the 2-D models, the detachment of 3-D slabs occurs within young lithosphere before the approach of the spreading ridge axis within ~ 100 km of the trench. Lateral variations in detachment timing and geometry depend on effects of lateral thermal and strength differences. In the case including offset ridge segments within the subducting plate (model 3d2), the transfer of slab pull between slab segments leads to more complicated dynamics involving tear propagation.

Table 2. Model Parameters and Results^a

Model	Parameters		Results					
	LatX	$x_{0,RT}$ (km)	t_{det} (Myr)	z_{det} (km)	$x_{d,RT}$ (km)	x_{TD} (km)	v_{avg}, v_{max} (cm/yr)	$A_{det,tr}$ (Myr)
Model 2dA		−300	5.20	90	−126	283	7.5, 8.5	10.3
Model 2dB		−450	6.56	85	−160	281	9.0, 9.8	10.6
Model 3d1	N150	na	na	na	na	na	2.2, 2.6	na
	N115	−300	7.91	39	−103	189	5.2, 5.7	8.0
	N75	−300	7.84	51	−111	192	5.2, 5.7	8.5
	N50	−300	7.68	44	−114	194	5.2, 5.7	8.2
	N0	−300	7.98	53	−114	223	5.2, 5.7	8.6
Model 3d2	A150	−300	6.94	74	−126	183	2.2, 2.6	11.2
	A100	−300	6.65	40	−134	189	5.0, 5.5	9.6
	A75	−300	6.65	43	−138	192	5.1, 5.6	9.7
	A50	−300	6.72	48	−138	197	5.1, 5.6	9.8
	0	na	4.14	77	na	239	5.1, 5.8	na
	B50	−450	5.94	48	−263	203	5.3, 6.0	16.1
	B75	−450	6.16	47	−273	192	5.3, 5.9	16.1
	B100	−450	6.16	40	−273	186	5.3, 5.9	15.8
	B150	−450	7.02	95	−263	172	2.3, 2.7	17.4
Model 3d3	A150	−300	na	na	na	na	2.2, 2.6	na
	A100	−300	7.25	46	−114	194	5.5, 6.5	8.6
	A75	−300	7.25	45	−120	194	5.5, 6.4	8.6
	A50	−300	7.25	45	−120	197	5.5, 6.4	8.6
	A25	na	6.84	49	na	200	5.4, 6.4	na
	0	na	7.04	56	na	197	5.5, 6.4	na
	B50	−450	6.90	49	−235	194	5.4, 6.4	14.8
	B75	−450	6.84	45	−235	192	5.4, 6.4	14.7
	B100	−450	6.90	44	−235	189	5.4, 6.4	14.6
	B150	−450	7.92	91	−226	181	2.5, 2.9	17.9

^aColumn LatX lists the latitudes at which results for trench-perpendicular cross sections of the 3-D slabs are presented (numbering indicates distance in km from the central latitude, “N” referring to northern latitudes for model 3d1 and “A” and “B” indicating cross sections of plate/slab A and plate/slab B, respectively, for model 3d2 or 3d3). Latitude A25 (bold) is included only for model 3d3 and discussed in the text. $x_{0,RT}$ is the initial ridge-trench distance, t_{det} is the detachment time (time $t = 0$ corresponds to the start of the model run), z_{det} is the detachment depth, $x_{d,RT}$ is the ridge abandonment distance from the trench, x_{TD} is the horizontal distance from the trench to the point above the slab gap, v_{avg} , v_{max} are the average and maximum subduction velocities, and $A_{det,tr}$ is the age of the lithosphere at the detachment point at the time it had encountered the trench. Detachment geometry is determined by the point of separation of the 1050°C temperature contour of the slab from the surface plate, and a listing of “na” indicates a latitude at which the slab is too warm to define some results for detachment according to that contour (i.e., model 3d1, latitude N150) and/or is located within a transform weak region that prevents reference to a distinct outboard ridge position (i.e., model 3d2, latitude 0).

3.1. Three-Dimensional Ridge-Trench Collision: Single Ridge Segment (Model 3d1)

[24] The time-dependent evolution for model 3d1 is illustrated by a sequence of four views of the 1050°C temperature isosurface during subduction, ridge migration, and the slab detachment process (Figure 3; see also Animation S1 and closeup Animation S2).¹ Time is given in million years (Myr) from the start of the model run (Figure 1b shows time 0 Myr for model 3d1 when the ridge is initially 300 km outboard of the trench). The early dynamics (Figures 3a and 3b) consists of the onset of subduction by the pull of the preexisting

slab, settling of the slab into a more vertical profile, subduction at a steady rate of ~5.5 cm/yr (see Figure 4a, model 3d1), and uniform ridge migration. The ridge and plate migrate together with very minimal latitudinal variation in ridge position and subduction velocity. At 6.5 Myr, when the ridge is within 150 km of the trench, subduction begins to slow (Figure 4a, model 3d1) as boudinage-type “necking” of the slab reduces the ability of the subducted plate to transmit pull to the surface plate. At 7.8 Myr, detachment gaps open within the slab in the form of multiple widening holes (Figure 3c; see also Animation S2). By 8.0 Myr the slab has completely detached (1.5 Myr since the slowdown of subduction began) at a depth of 40–50 km depth along the center and leaving two slightly deeper detachment nubs where the northern and south-

¹Auxiliary materials are available in the HTML. doi:10.1029/2010GC003286.

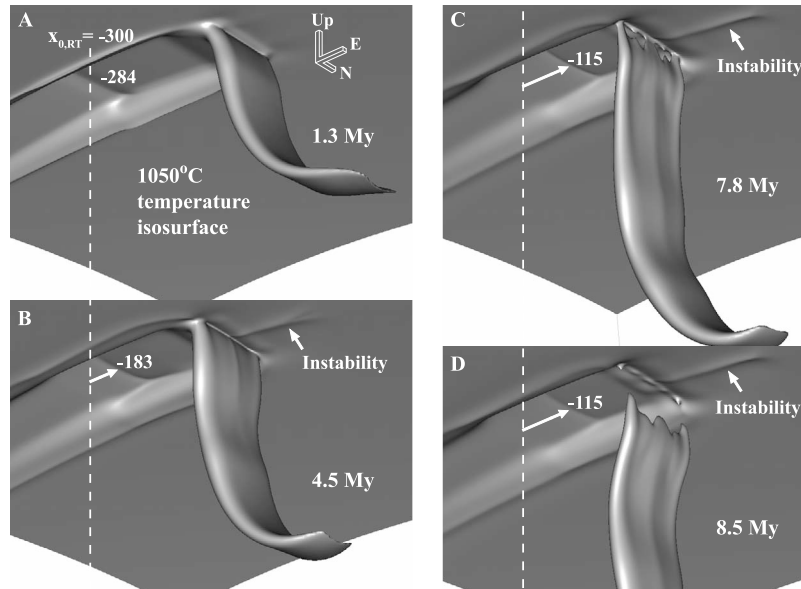


Figure 3. Time sequence of dynamics for model 3d1. The 1050°C temperature isosurface outlines the temperature structure of the subducted slab and the ridge within the subducting plate and shows the dynamics by way of changing morphology at four times (indicated in Myr in each frame). As indicated with the directional marker shown in the top right of Figure 3a, the view is looking upward from the interior of the Earth beneath the slab and the underside of the ridge. (a) Sinking of the slab to a more vertical profile than prescribed by the initial structure (see Figure 1b), ridge ~284 km outboard of trench; (b) subduction (~5.6 cm/yr) and ridge migration (ridge ~183 km outboard); (c) detachment central to the slab (~190–205 km inboard, 45–75 km depth), subduction ~0.4 cm/yr and approaching zero, and abandonment of ridge ~115 km outboard; and (d) sinking of completely detached slab and cooling of abandoned ridge.

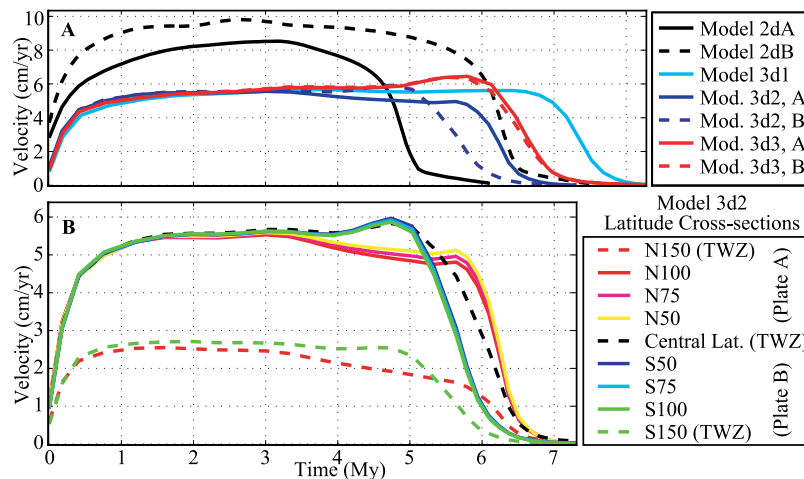


Figure 4. Subducting plate velocity as a function of time. (a) Comparisons between 2-D models (black) and central latitudes of plate segments in 3-D models (colored lines). Solid lines are for models or cross sections with an initial ridge position of 300 km, and dashed lines are for an initial ridge 450 km outboard of the trench. For models 3d2 and 3d3 that have two plate segments, “A” next to the model name indicates latitude cross section N75 across plate A, and “B” indicates cross section S75 across plate B. (b) Comparison between subduction velocity curves for latitude cross sections of model 3d2. Dashed lines are at latitudes within or at the edge of the transform weak zones (TWZ), warm colors represent northern latitude cross sections of plate A, and cool colors represent southern latitudes across plate B.

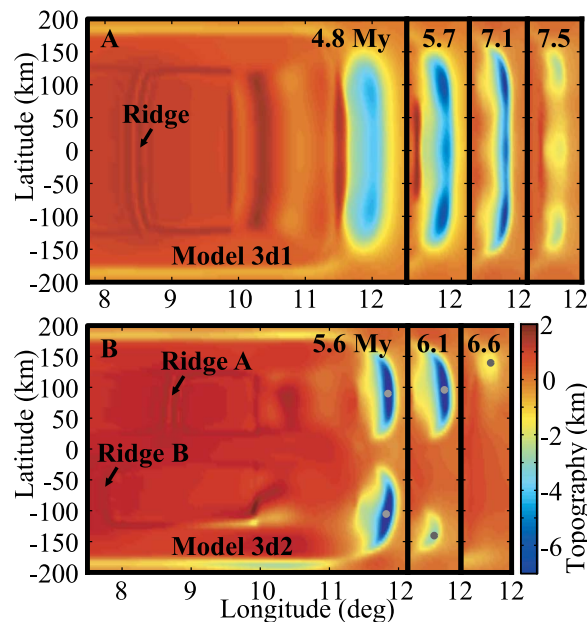


Figure 5. Map views of dynamic topography at multiple times for (a) model 3d1 and (b) model 3d2. Colors represent topography ranging from highest elevation associated with the ridge (leftmost images only) and the lowest associated with the effect of slab sinking on the overriding plate. See the text for notes on the unrealistically large magnitudes and lack of trench topography in these models. The changes in topography for the narrower region above the slab are shown at later times within the images toward the right. Dynamic topography for model 3d2 (Figure 5b) includes grey points showing the position of the minimum topography above each of the slabs associated with the offset ridge/plate segments.

ernmost edges of the slab detached (Figure 3d). Upon detachment, the subduction velocity converges to zero (Figure 4a, model 3d1), and the ridge has been abandoned ~100–115 km outboard of the trench.

3.1.1. Detachment Central to Slab, No Propagation

[25] An important aspect of model 3d1 is that the location of detachment is *central* to the slab and almost simultaneous along the subduction zone. This is contrary to tear initiation at slab edges and propagation in a particular direction as commonly discussed in detachment studies. Although few occurrences of slab detachment in the Earth are likely to be perfectly symmetric, it is important to recognize the possibility of detachment initiation central to subducted slabs.

[26] The detachment process in detail includes slight latitudinal differences in the timing of detachment (a maximum difference of 0.3 Myr) through the occurrence of multiple holes opening central to the slab. However, the process is nearly simultaneous along the trench, considering the rapid necking and that there is no consistent lateral propagation of detachment. The lateral symmetry and uniformity of the thermal structure allows the subducted slab to exert a nearly uniform slab pull along the subduction zone, with the exception of a slight difference at the warmer edges. The difference in detachment depth and timing at either edge of the slab is due to the slightly slower and deeper detachment of the warmer edges of the subducted slab compared to the plastic yielding of the colder central section of the slab. This is consistent with the results of 2-D models [Andrews and Billen, 2009] demonstrating that warmer lithosphere allows stretching to delay and deepen detachment, whereas colder, stronger lithosphere detaches more quickly and sharply (with a shorter remnant nub) by plastic yielding.

3.1.2. Topography Reflects Detachment Timing and Location

[27] Changes in dynamic topography at the surface above the slab reflect the spatial and temporal effects of slab pull, particularly during the loss of coupling to the slab during detachment. Although magnitudes of topography in these models are likely higher than expected in the real Earth based on the olivine-only rheology, the changes with time reflect the underlying dynamics independent of total magnitudes. The focus here is therefore largely on the temporal and spatial changes.

[28] The topography for model 3d1 consists of elevated topography associated with the approaching spreading ridge, and a trench-parallel low region within the overriding lithosphere above the subducting slab (Figure 5a). The regional low narrows, deepens, and shifts westward as the progressively warmer slab retreats into a more vertical profile and focuses slab pull more locally until detachment leads to its rapid decrease and disappearance (Figure 5a). This topographic evolution is consistent with the sharp break-off signal and subsequent rebound seen in dynamic 2-D models [Burkett and Billen, 2009; Duretz et al., 2010]. Within the 3-D models, slight variations along strike arise as focused lateral regions of deeper topography at the center and edges of the slab (Figure 5a), which correspond to the locations at

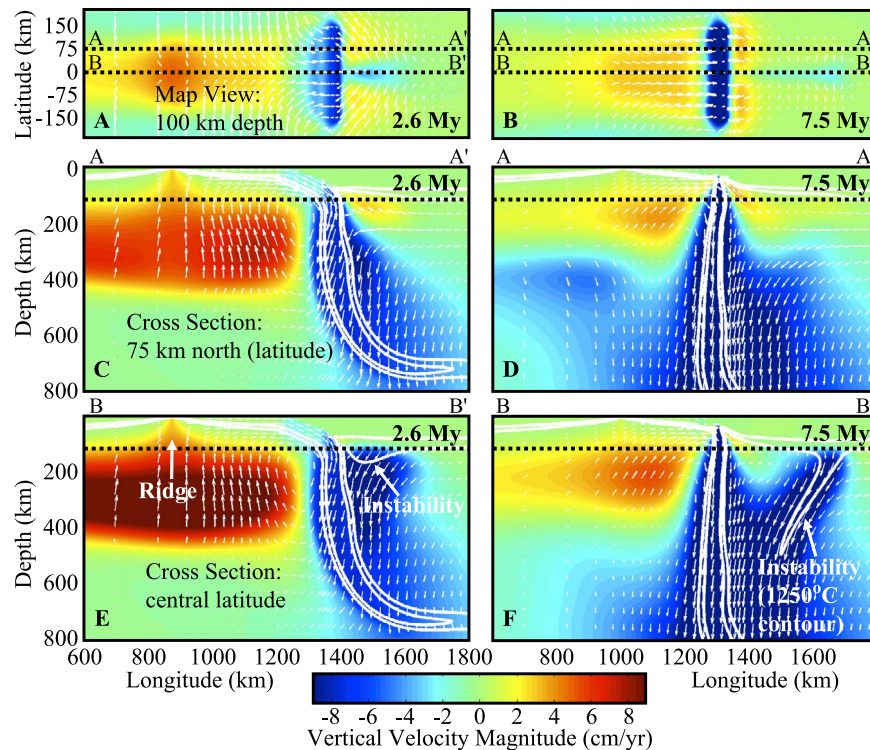


Figure 6. Flow field and vertical velocity magnitude for model 3d1. The slab and ridge are outlined in white by the 1050°C and 1250°C temperature contours. The 1250°C temperature contour also outlines the Rayleigh-Taylor instability at the central latitude (Figures 6e and 6f). Map views (at 100 km depth) of flow field (white arrows) and vertical magnitude of velocity (colors) at a time (a) during subduction and (b) during detachment. (c–f) Cross sections with depth along the profiles shown by dotted lines in the corresponding map view plot. Note that the color bar values saturate at ± 9 cm/yr to better show variations in magnitudes around the detaching slab, although values actually range between -14 to 11 cm/yr.

which detachment occurs later compared to the regions in between where detachment first occurs in the form of opening holes within the slab (Figure 3c).

[29] Note that the trench (at 10° in longitude) is no longer visible as a distinct minimum in topography (Figure 5a) because spreading ridge approach is associated with a decrease in trench depth and eventual elimination of the dynamic trench topography, consistent with observed correlations of trench depth with age of the subducting lithosphere [Grellet and Dubois, 1982] and previous 2-D modeling of ridge-trench collision [Burkett and Billen, 2009].

3.1.3. Three-Dimensional Mantle Flow Patterns

[30] Three-dimensional flow patterns illustrate the interactions between mantle flow, slab morphol-

ogy, and thermal structures of the overriding and surrounding plates. The large-scale flow during subduction is characterized by downward flow associated with the sinking slab and upward flow behind the slab that is focused toward the ridge (Figures 6a, 6c, 6e, and 7a). This pattern is nearly identical to that found in the 2-D models, although magnitudes are smaller in 3-D than 2-D (see also section 3.4). During detachment, vertical flow is diverted away from the ridge, as subduction and ridge-trench migration cease, and focuses instead around the necking and detaching slab (Figures 6c and 6e versus Figures 6d and 6f). After detachment, flow is focused upward through the detachment gap, with velocities up to 10 cm/yr, and entrained after the sinking slab (Figure 7c).

[31] In the lateral dimension, the sinking and retreating slab draws material around its lateral edges such that the flow rotates around the slab edges and is entrained after the sinking slab (Figure 7a, bottom

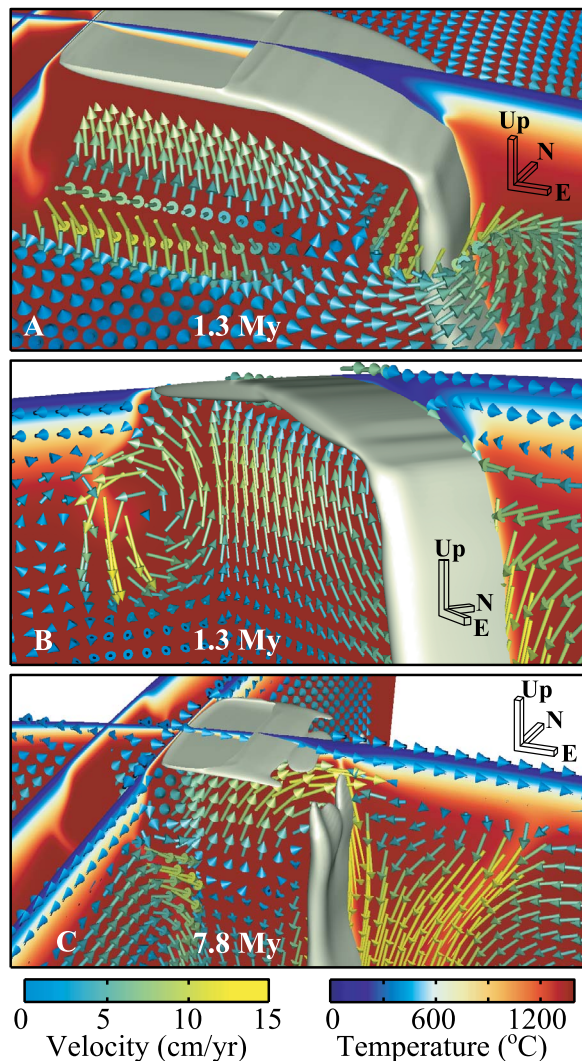


Figure 7. Flow field dynamics of ridge-trench collision and detachment. A viscosity isosurface (5×10^{21} Pa s) is shown only for the subducting plate to allow a clear view of surrounding flow patterns. Arrow sheets indicate instantaneous flow direction, with colors corresponding to magnitudes of velocity indicated in the corresponding blue to yellow color bar. Vertical slices of temperature bifurcating the slab and cutting parallel behind the ridge show the variations in thermal structure. The representative general flow pattern for subduction and ridge migration characterized by (a) flow driven downward and around the front of the sinking and retreating slab and (b) return flow concentrated upward toward the migrating ridge, with an outward (in latitude) rotational pattern. (c) At detachment, flow is no longer focused upward at the abandoned ridge but is instead diverted upward toward and through the slab gap and downward after the sinking slab.

right-hand corner). The lateral jump in lithospheric depth between the thin lithosphere near the ridge and the background plate also causes a rotational pattern as flow is directed upward beneath the center of the ridge and then rotates outward in latitude, while eroding the base of the thicker surrounding lithosphere (Figure 7b, top left).

[32] The flow above the center of the sinking slab also causes the focused erosion of a Rayleigh-Taylor instability from the base of the overriding lithosphere that is entrained after the sinking slab (Figures 7c, 6e, and 6f). The instability is limited to the central latitude and causes a ridge (downward temperature isosurface deflection) along the top of the slab and beneath the overriding plate (see Figures 3b–3d). The slightly later detachment of the center of slab may be caused in part by the thermal thickening of the plate associated with the instability and its related flow pattern.

3.1.4. Vertical Flow Through Slab Gaps

[33] Since melting is not incorporated into the models presented here, the vertically upward component of velocity may be used as a proxy for decompression melting that might result from the dynamics. As seen in 2-D model results, the region of localized upward flow within the mantle wedge shifts trenchward and to shallower depths during subduction of progressively thinner lithosphere once the ridge approaches within 200 km of the trench and as the slab begins the necking process leading to detachment (Figures 8a–8d). There are slight variations in the magnitudes of vertical flow laterally along the subduction zone with time (Figure 8e), which depend on the along-strike differences in detachment timing. Regions of greater magnitudes of upward flow along strike correspond to actively detaching lithosphere, whereas vertical flow rapidly ceases within ~ 0.1 Myr where detachment gaps have opened within the slab and flow is instead entrained downward after the sinking slab.

3.2. Three-Dimensional Ridge-Trench Collision: Two Offset Ridge Segments (Model 3d2)

[34] Unlike the previous symmetric case of nearly uniform slab pull along the trench, the lateral variation in thermal structure of the slab in model 3d2 leads to more complicated interactions between the plate segments due to spatial transfer of slab pull along the subduction zone. In particular, detachment can occur in older lithosphere as slab pull

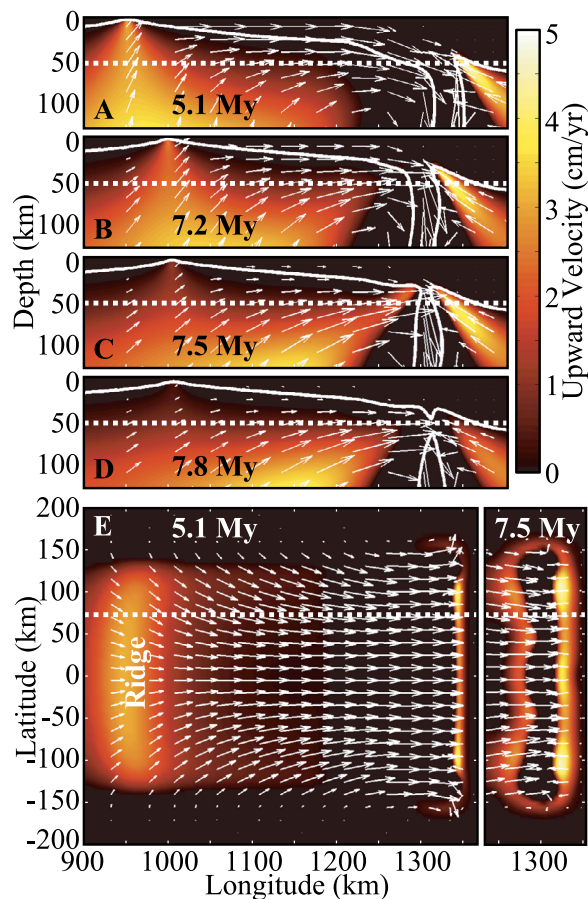


Figure 8. Flow field and upward-only component of velocity for model 3d1. Arrows indicate flow field, and colors represent the magnitude of the upward-only component of velocity (black is 0 and downward). Trench-perpendicular cross section at 75 km latitude at four times showing (a) subduction, (b) ridge migration and shallowing of flow in wedge, (c) focusing of upward flow around necking slab, and (d) diminishing upward flow after detachment. (e) Map views of the flow field and vertical velocity component at 50 km depth for times also shown in Figures 8a and 8c. The dotted line corresponds to the depth and latitude where the planes of view shown in Figures 8a–8d intersect with map view (Figure 8e).

forces are transferred from one plate segment to another. Observable changes of the subduction velocity and topography at the surface also reflect the transfer of pull from one surface plate segment to another during and after lateral propagation of detachment. The time evolution of model 3d2 is illustrated with a time sequence of eight views of the 1050°C temperature isosurface during the subduction, ridge migration, and laterally propagating slab detachment of the two offset ridge segments (Figure 9; see also Animation S3).

3.2.1. Initial Dynamics and Vertical Tearing

[35] The evolution of model 3d2 begins with laterally uniform subduction at ~ 5.5 cm/yr for the first 3 Myr as shown by the identical subduction velocity history curves at this time (Figure 4b) for all latitudes with the exception of the northernmost and southernmost cross sections, where subduction is slowed by the coupling across the transform weak zones. The trench-parallel subduction velocity at 3.0 Myr also illustrates the early lateral uniformity of subduction across both plate segments preceding this time (Figure 2). Starting at 4.1 Myr, however, a vertical gap opens between the slab segments at 77 km depth and propagates vertically downward (Figures 9b and 9c). The separation allows the plate segments to subduct more independently of each other as reflected by the divergence in the subduction velocities of plates A and B with time after 3 Myr (Figure 4b) and the increased lateral offset in velocity between the two segments (Figure 2). The presence of the transform weak zone facilitates the opening of the vertical slab gap by allowing more thinning of the lithosphere by thermal erosion within the weakened zone. The thermal effect is then maintained as part of the slab structure between the plates even after the slab has subducted beyond the reach of the direct effect of the imposed transform weak zone (below 110 km depth).

[36] Both slab segments remain attached to the surface plate up to ~ 5 Myr, despite a difference in subduction velocity of up to 1 cm/yr for the ~ 1 –2 Myr prior to the beginning of detachment. This is made possible in part by stretching at shallow depths of the warmer subducting slab A, which reduces the slab pull on the surface plate segment as reflected in the decrease in subduction velocity by ~ 0.5 cm/yr from ~ 3.5 –5.5 Myr (Figure 4b, north latitude profiles). Meanwhile, the component of slab pull no longer transmitted to plate A during stretching is transferred to plate B, and a brief acceleration in the subduction velocity occurs just prior to detachment (Figure 4b, south latitude profiles between ~ 4 –5 Myr).

3.2.2. Horizontal Propagation of Detachment

[37] The detachment of slab B occurs by way of propagation of detachment from north to south, parallel to the subduction zone (Figures 9c–9h). The propagation occurs rapidly at a rate of at least 100 km/Myr and completely detaches slab B within ~ 1 Myr. The detachment occurs at depths of ~ 40 –50 km with the exception of a deeper 95 km remnant nub at the southernmost detached edge (see

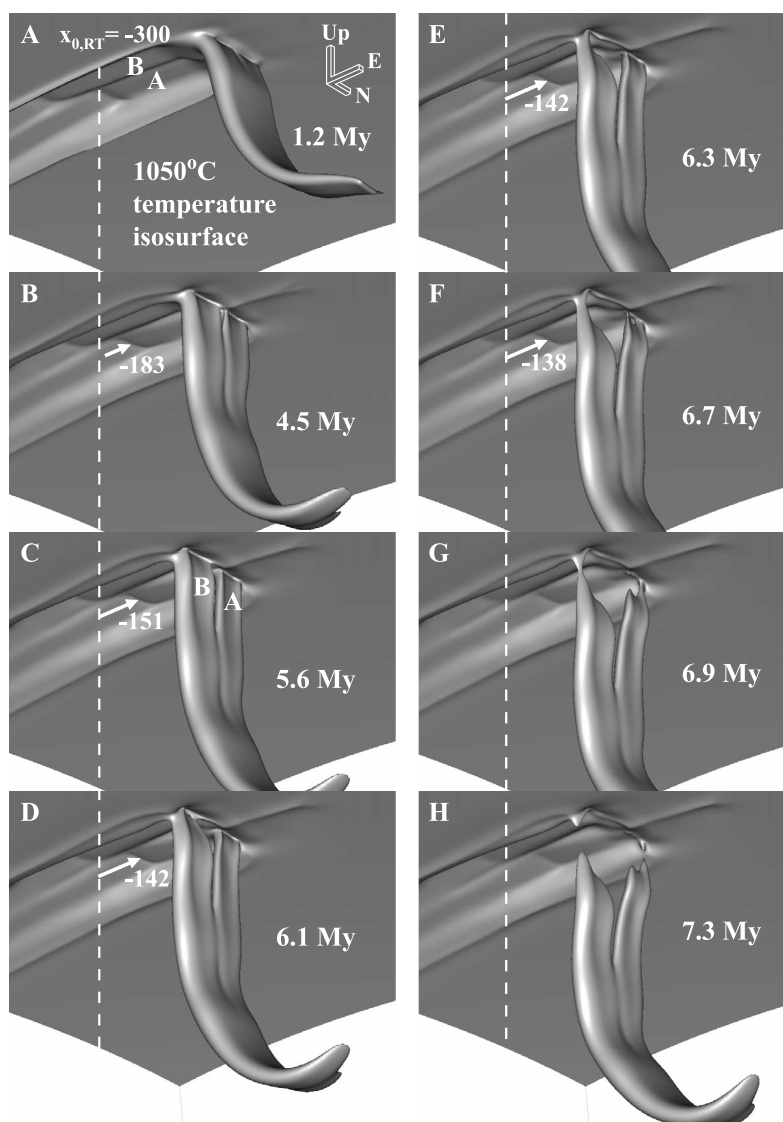


Figure 9. Time sequence of dynamics for model 3d2. The 1050°C temperature isosurface outlines the subducted slab and temperature structure of the offset ridge segments and associated plates, labeled A and B. (a) Early subduction and sinking of slab to vertical, (b) initiation of a vertical slab gap between the two plate segments, (c) downward propagation of the vertical slab tear, (d) horizontal propagation of tearing across slab B, (e) stretching of slab A during horizontal detachment of slab B, (f) initiation of detachment of slab A central to the slab, (g) horizontal detachment of slab A during finishing detachment of slab B, and (h) complete detachment and sinking.

Table 2, model 3d2 latitude cross-section results for details of the detachment depths and timing). As slab B detaches, evidence for the transfer of its negative buoyancy to plate A at about 5.25 Myr can be seen in the sudden leveling off in plate A subduction velocities, followed by a slight speed-up just before detachment of slab A begins (Figure 4b).

[38] The detachment of slab A, on the other hand, mainly propagates south to north, although the detachment first occurs as an opening hole (Figure 9f) at latitude A75. Because slab A is younger and warmer, it accommodate more stretching during

the detachment process, particularly at the warmer edges, while the central hole opens earliest in the slab where deformation of the colder interior of the slab is controlled by plastic yielding. Although the detachment does propagate northward from the initial hole interior to the slab (Figures 9f–9h), the overall detachment resembles more of the stretching “boudinage” type detachment occurring in model 3d1.

[39] The difference in detachment between slabs A and B reflects the importance of plastic yielding in the detachment process. Detachment of an older (or

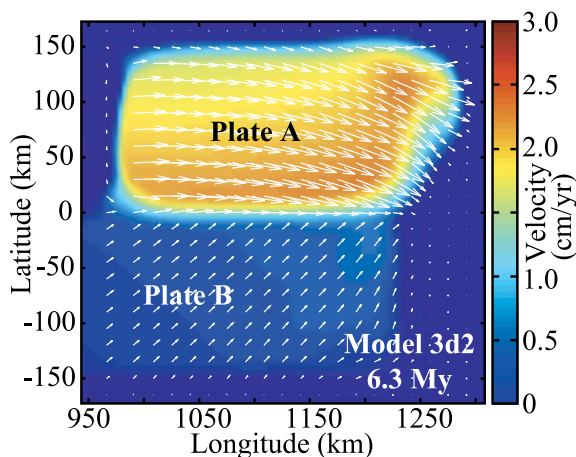


Figure 10. Map view of surface plate velocity direction and magnitude for model 3d2 at 6.3 Myr. Colors represent velocity magnitude (cm/yr), and white arrows indicate instantaneous flow direction.

stronger) slab, as in the case of slab B in model 3d2, can develop rapidly and demonstrate clear single-directional horizontal propagation of slab detachment. In contrast, a warmer slab in the case of model 3d1 or slab A in model 3d2 can more easily accommodate a component of slab pull by stretching, and the detachment process is more laterally distributed in the form of holes opening central to the slab (Figures 3c and 9f), with delayed detachment time (Figure 4a, model 3d1 and model 3d2 ridge A versus model 3d2 ridge B).

3.2.3. Differential Subduction Velocities Across and Along Ridge Segments

[40] An interesting aspect of model 3d2 is the separation in dynamics of the two plate segments across the central transform weak zone. During the detachment of slab B, for instance, the subduction velocity between plates A and B reaches a maximum difference of up to 3 cm/yr (Figure 2, 5.9 Myr profile). Then the velocity of plate B drops to zero and plate A continues to pull the surface plate for another 1 Myr before it also completely detaches.

[41] In addition to differences between ridge segments, there are also lateral variations in the subduction velocity interior to each of the plate segments, as demonstrated by linear increases in subduction velocity of each plate segment inward toward the central transform weak zone, most obvious in the subduction velocity profiles at 4.5 and 5.9 Myr (Figure 2). The faster velocity closer to the center of the subduction zone corresponds to

the greater slab pull originating from the deep central portion of the slab where slab A and B are still joined. The innermost parts of each slab are also more closely coupled to pull from the opposite segmented slab, and the outer edges are slowed by viscous drag along the transform weak zones. This effect can also be seen in a map view of the velocities indicating rotational motion within plate A toward the southern end of the subduction zone where slab pull is increased by additional pull of detaching slab B (Figure 10).

3.2.4. Topography Mirrors Propagating Detachment

[42] The positioning of the deepest point in topography associated with each of the subducting segments in model 3d2 is a useful measure of the location of maximum slab pull and tracks the position of the propagating detachment at depth. In model 3d2, there is initially a central focus of the minimum topography above the center of the continuous single slab, but separate minimums associated with each of the slabs quickly shift laterally to positions above the centers of the associated slab (Figure 5b). After 5.5 Myr, the propagation of detachment in latitude for both segments is also mirrored by propagation of the minimum topography (Figure 5b).

3.2.5. Central Transform Weak Zone: Active Within Subduction Zone (Model 3d2) Versus “Healed” Outboard of Trench (Model 3d3)

[43] Because the strength of fracture zones is currently unknown, it is important to separately understand the effect of the fully weakened central transform weak zone extending through the subduction zone in model 3d2. For comparison, we present model 3d3 in which the only difference from model 3d2 is that the central transform weak zone is effective between plates A and B only to 50 km outboard of the trench (see Figure 1c). The plate has effectively viscously “healed” before entering the trench, although it retains the effective weakening effects along this zone caused by thermal thinning of the lithosphere along the transform weak zone.

[44] The effect of the increased coupling between plates A and B just outboard of the trench and within the subduction zone is to join the two as if they are a single plate and slab, as evident in the subduction velocity history, which demonstrates nearly identical subduction velocity across both

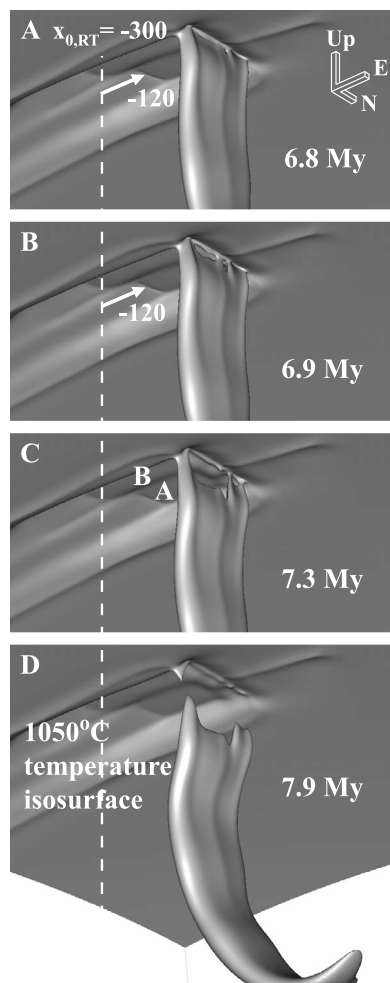


Figure 11. Time sequence of dynamics for model 3d3. Frames are shown only for times at which the slab morphology differs noticeably from model 3d2 dynamics. (a) Earliest initiation of detachment, (b) detachment through center of slab B, (c) detachment within center of slab A, and (d) complete detachment and sinking.

plate segments (Figure 4a). Slab B still detaches before slab A as in model 3d2 (Figure 11; see detachment times, Table 2), but the detachment is nearly simultaneous across each segment rather than demonstrating horizontal propagation as in model 3d2 (Figure 11; see also Animation S4). Although a small hole is first to open between the two segments at a depth of 49 km while slab A undergoes stretching and slab B detachment begins (Figures 11a and 11b; see Table 2, additional latitude A25 for model 3d3), there is no extensive vertical opening of a slab gap between the segments along the transform-weakened and age offset boundary as seen in model 3d2.

[45] Overall, in comparison to model 3d2, the results of model 3d3 clearly illustrate the impor-

tance of a weak transform boundary between ridge segments within the subduction zone (included in model 3d2) for the development of a vertical separation between slab segments that enables the segmented plates to move independently and subduct with differing velocities. Such decoupling of the slab segments allows more complicated lateral transfers in slab pull that can lead to horizontally propagating slab detachment.

3.3. Consistency of 3-D Results With 2-D Detachment

[46] Although there are lateral variations in the detachment process within the 3-D models, the first-order rheologic properties controlling detachment in the 2-D models are also responsible for detachment in 3-D, and the added effects of 3-D geometry modify how these processes control the deformation. Detachment during ridge-trench collision occurs by plastic yielding of the slab interior. The yielding process occurs quickly if greater slab pull forces initiate detachment in older and/or stronger lithosphere. For younger and/or warmer lithosphere, detachment occurs more slowly by accommodating a component of the deformation through stretching. The detachment occurs at a lithospheric age (calculated as by *Burkett and Billen* [2009]) between 8 and 11 Myr for model 3d1 and slab A in model 3d2, which is consistent with the range in age at the point of detachment of 7–12 Myr found in 2-D results [*Burkett and Billen*, 2009]. The detachment of slab B at a slightly older age is attributed to additional effects of the 3-D geometry through lateral transfer of slab pull from the adjacent slab segment (discussed below).

3.4. Divergence From 2-D Detachment Results

[47] The 2-D model results predict detachment in ~10 Myr old lithosphere for the slab segment with the closest ridge to the trench. The results of model 3d2 indicate, however, that the process of lateral transfer in slab pull can lead to more complicated variation and tradeoffs along the subduction zone. Based on the expectation from the 2-D results, the closer ridge segment (ridge A) should cause detachment of slab A before slab B; therefore, the detachment of slab B before slab A is initially surprising. However, a closer look at the time-varying transfer of slab pull laterally between the slabs and to the surface plates reveals the distinctly 3-D nature of this nonsymmetric case of ridge-trench collision. The detachment of slab B through



lithosphere ~5 Myr older than in the 2-D case (~16–17 Myr versus 10.6 Myr) is due to the 3-D effect of transferring slab pull from slab A to slab B, which causes stress in slab B to exceed the yield strength earlier and within older, stronger lithosphere than in the 2-D case.

[48] The overall subduction dynamics in 3-D also differs from 2-D in that the subduction velocities are nearly twice as fast in the 2D models. 2-D models 2dA and 2dB reach subduction velocities between 8 and 10 cm/yr whereas the maximum 3-D model subduction velocity is 6 cm/yr (Figure 4a). While viscous resistance to subduction from the mantle and through coupling along the shear zone create nearly the same per-unit-latitude effect in the 3-D models as in the 2-D models, the addition of lateral viscous drag along the transform weak zones can account for slower subduction in 3-D. The positioning in latitude of the transform weak zones and decrease in subduction velocity distributed across the zones indicate the effect of viscous drag, which acts to slow the plate velocity (Figure 2).

4. Discussion

[49] The 3-D model results presented here demonstrate that, as in 2-D models, ridge approach leads to a slowdown of subduction followed by detachment within young, weak lithosphere. The detachment process occurs in the form of “boudinage”-type necking of the slab, a mode of detachment that has been observed recently, for instance, in the seismicity (clustering of hypocentral locations and fault plane orientations) of a subducted slablet beneath the Hindu Kush within the India-Asia collision zone [Lister *et al.*, 2008]. A similar pattern in seismicity beneath the Vrancea region has been linked to viscous stresses associated with a detaching relic oceanic slab [Ismail-Zadeh *et al.*, 2000]. Tomographic imaging of the Pacific slab beneath Japan also provides evidence for slab thinning to the north, which has less wave speed contrast compared to wave speed anomalies at the southern end of the Izu-Bonin arc where a horizontal tear is more clearly recognized within the slab [Kennett and Furumura, 2010]. Although such seismic imaging of the potentially early or recent detachment is rare due to the brief and spatially narrow nature of the process, the improvement of seismic imaging techniques with higher resolution and greater regional coverage will likely continue to resolve subducted slab structures to allow better recognition of the finer details of slab gaps and tears.

[50] Even on a larger scale, recent high-resolution tomographic imaging of the mantle beneath North America, for instance, reveals previously unrecognized complexity of the subducted Farallon plate structure, including large tears that might be linked to unusual volcanism of the Laramide era [Sigloch *et al.*, 2008]. Such observations necessitate re-evaluations of current models of the regional subduction history and, in general, call for a better understanding of slab tearing to determine the effect of fragmentation of subducted slabs on surface deformation and processes leading to the distributions and recycling of slab material within the mantle.

[51] Contrary to hypotheses in studies mentioning 3-D slab detachment and assuming tears originate at the edges of slabs [Wortel and Spakman, 2000; Yoshioka and Wortel, 1995], results of model 3d1 and segment A in model 3d2 demonstrate that slabs may instead begin detaching within the center, as controlled by plastic yielding of the colder central region of the slab, which outpaces detachment of warmer lithosphere (e.g., at lateral edges) that can accommodate deformation by stretching. Even though there is less viscous support of the edges of the slab due to the low-viscosity mantle, the detachment does not initiate at the edge, which indicates that it is indeed the slab strength and not the viscous drag on the slab that controls where detachment occurs. Model 3d1 also demonstrates nearly simultaneous detachment along latitude, and together with the occurrence of detachment in the form of holes opening central to the slab, forms a picture of the occurrence of detachment that has not yet been recognized but should be considered in future studies of slab detachment.

[52] Although detachment may not be restricted to initiation at slab edges and might occur simultaneously along strike in some cases, results of model 3d2 and observations of propagating magmatism and uplift also provide evidence for lateral propagation of slab detachment. Along the North, Central, and South American plate margin there are a number of locations where slab window volcanism may have been caused by horizontal slab detachment, but a clear directional propagation of detachment is not equally obvious in all examples. Proposed south-east propagation of detachment based on a clear age progression in magmatism within the Trans-Mexican Volcanic Belt, for instance, may track the process of lateral slab tear propagation at a rate of 100–250 km/Myr through central Mexico [Ferrari, 2004], comparable to the ~100 km/Myr rate of tearing of slab B in model 3d2. Ferrari [2004]



proposes initiation of the tear in the Baja California region, where the abandonment of ridge segments together with postsubduction slab gap volcanism also provides evidence for detachment at ~12 Myr [e.g., *Pallares et al.*, 2007]. Along Baja California, however, the nearly concomitant eruption of anomalous magmatism linked to detachment between 26 and 30°N is interpreted as evidence for very rapid north to south propagation [*Pallares et al.*, 2007; *Michaud et al.*, 2006], whereas simultaneous detachment and opening of slab gaps across a number of slab segments may also be consistent with observations for some sections of the margin.

[53] A similar lack in correlation of the timing of volcanism with latitude is also used to argue for very rapid propagation of detachment across slab segments entering the trench at the Chile Triple Junction [*Guivel et al.*, 2006]. Such detachment may be consistent with rapid tear propagation as seen in detachment of the slab segments in model 3d2, or the timing may alternatively be consistent with simultaneous detachment within each slab segment, with northward propagation in magmatism tracking the northward migrating location of ridge-trench collision (of multiple occurrences of each detaching slab segment) rather than northward propagation of a single tear. In general, the current conceptual view of tear propagation initiating in one region and migrating for great distances along a slab should be cautiously balanced with a consideration of the possibility that detachment may initiate independently or simultaneously along strike and may not require a slab edge or preexisting tear.

[54] Lateral propagation of slab detachment has been linked to southeast shifts in foredeep depocenters along Italy tracking migration in focused slab pull at the edge of a tear in the Adriatic slab [*van der Meulen et al.*, 1998]. Such migration in the topographic expression of slab detachment is consistent with results of migrating deepest points in topography above the detaching slabs in model 3d2. The observed propagation of topographic effects is, however, in the form of stepwise shifts in depocenters that maintain their positioning for a couple million years and migrate at a slower propagation rate an order of magnitude slower than propagation within the models presented here. The detachment is, however, within older lithosphere, and the propagation of detachment is expected to be faster within the thin, young lithosphere of the slabs in these models.

[55] Vertical tear propagation may be another form of slab tearing that might initiate from a lateral

difference in thermal structure within a subducted slab, along with previous weakening between the plate segments from the presence of a transform fault or fracture zone. Coupling across transform faults may increase during the transition into fracture zones [*Wessel and Haxby*, 1990], but such strengthening of the zone may not be able to reverse effects of earlier thermal or viscous erosion and thinning of the thermal lithosphere when the zone was weaker. For instance, viscoelastoplastic modeling results by *Hall and Gurnis* [2005] show the removal of ~15 km of thermal lithosphere beneath a fracture zone (a process also observed beneath the transform weak zones in model 3d2), in addition to evidence for low depth-averaged yield strength (<10 MPa) in order to match profiles of bathymetry and gravity across the zones. More recent studies have also found fracture zones to be partially serpentinized, and therefore weak, for hundreds of kilometers along the zone and possibly to depths nearly through the oceanic lithosphere [e.g., *Manea and Manea*, 2008]. A low strength of fracture zones may be important in opening of a vertical slab gap and allowing independent motion between adjacent age offset slab segments and horizontally propagating detachment, as seen in model 3d2. The opening of a slab gap between plate segments may be observed, for instance, in the seismic structure beneath western Mexico, where a recent tomographic model by *Yang et al.* [2009] shows a clear vertical gap between the Rivera and Cocos slabs below 150 km depth, across which there is a change in dip between the slabs.

[56] Without a weak transform fault zone within the subduction zone, as demonstrated by results of model 3d3 in which the transform fault zone had effectively healed upon entering the trench, the dynamics consist of lateral uniformity of subduction as the offset plate segments move as a single joined plate. Observations of the rotation and fragmentation of real ridge segments may be more consistent with model 3d2 results in which fracture zones remain weak through the subduction zone during ridge-trench approach.

[57] Implications of model 3d2 for the breakup and rotation of a ridge during approach to a subduction zone comes from the lateral variation in subduction velocity across each of the plate segments (Figure 2). In the models presented here, the viscous rheology and plasticity criterion do not allow a mechanism for dynamically acquired and maintained strain localization; therefore the plates cannot break up and form faults or develop new offsets in ridge segments. However, gradients in velocity across



the plate segments provide insight into the effects of ridge-trench collision and detachment on intra-plate deformation that might otherwise lead to rotations and breakup. For instance, at a time during detachment of slab B and just before detachment of slab A in model 3d2, a map view of the surface plate velocity directions and magnitudes (Figure 10) shows rotation of plate A as slab pull is transferred from the addition of negative buoyancy from detached slab B, which is particularly concentrated at the southern end of the plate A subduction zone. In the Earth, similar lateral variations in subduction velocity along a single plate segment may be observable in the rotation and fragmentation of ridge segments (e.g., breakup of the Farallon plate upon EPR approach to North America [Menard, 1978]).

[58] Some studies discuss the tearing of lithosphere due to rapid spatial changes in geometry along the subduction zone causing vertical tears, for instance, beneath the tightly curved Mariana arc [Miller *et al.*, 2006] and the Aleutian-Kamchatka junction [Yogodzinski *et al.*, 2001]. Tearing of lithosphere may also be important throughout the history of trench migration in the Mediterranean through the propagation of orogen-perpendicular lithospheric “tear faults” due to along-strike variation in slab rollback rate [e.g., Gasparon *et al.*, 2009]. Rollback is not permitted in the models presented here and therefore does not directly apply to these scenario, although vertical tear propagation along transform or fracture zones may produce similar tear geometry. Such tearing processes resulting from along-strike variation in subduction zone geometry and lateral differences in slab rollback are distinguishable from the models presented in this study that focus on the detachment associated with ridge-trench collision. However, a better understanding of the controls and dynamics associated with all modes of the tearing of lithosphere is necessary for a comprehensive view of slab and mantle rheology and the fate of subducted lithosphere.

[59] Despite the level of complexity that these 3-D models add to 2-D scenarios, there are limitations associated with the relatively simple 3-D geometries presented here. For instance, the 3-D models represent parallel ridge-trench collision, a choice necessary for comparison with 2-D results and as a first step in understanding the 3-D dynamics. The narrow slabs (150–300 km width) also limit potential comparison with the dynamics of detachment along much wider slabs, which may demonstrate lesser effects of flow around and thermal effects associated with the slab edges. The trans-

form weak zones, particularly the central zone separating the slabs in model 3d2, are wider than ideal for representing real faults. The dynamics therefore reflect the effects of wider distribution in stresses and velocity across these zones and a potentially wider gap opening vertically within the subducted slab in model 3d2 than might be expected in the Earth. In general, however, the design of the 3-D models here is an appropriate step toward increasing the realism of models while constraining the first-order controls on the dynamics of 3-D slab detachment.

5. Conclusions

[60] As in 2-D model results, the detachment of 3-D slabs occurs within young lithosphere before the approach of the spreading ridge axis within ~100 km of the trench. The 3-D detachment process can occur in the form of vertical and/or horizontal propagation of detachment, or may be nearly laterally simultaneous in the form of boudinage-type necking and opening of holes central to the slab. The initiation of detachment central to slab segments should be recognized as a plausible mode of detachment that has not yet been considered in previous studies of slab detachment. Center-initiating detachment is caused by the quicker detachment of plastically yielding lithosphere compared to detachment of warmer lithosphere, particularly at slab edges, which can accommodate deformation by stretching and thereby delay and deepen the process. Slab detachment in the form of a vertically propagating separation may initiate at an age offset boundary within a subducted slab that was previously weakened by the presence of a transform fault or fracture zone. Horizontally propagating detachment may also occur as a result of lateral transfers in slab pull between surface plate segments. Slab detachment is a rapid (~1 Myr) process, with tear propagation speeds up to ~100 km/Myr, and observations of changes in subduction velocities and topography with time provide a measurable surface manifestation of the dynamics of the deeper detachment process.

Acknowledgments

[61] This research was supported by the National Science Foundation (NSF) award EAR0337376 and also supported by NSF through TeraGrid resources provided by TACC under grant TG-EAR080014N (awarded to Magali Billen) and grant TG-MCA08T011 (awarded to Computational Infrastructure for Geodynamics (CIG)). We thank CIG for making the



CitcomCU software available and for awarding generous access to TeraGrid resources. We thank Oliver Kreylos and the KeckCAVES for developing the 3DVisualizer software used to visualize the 3-D model results. We thank T. V. Gerya and an anonymous reviewer for constructive comments.

References

- Andrews, E. R., and M. I. Billen (2009), Rheologic controls on the dynamics of slab detachment, *Tectonophysics*, **464**, 60–69, doi:10.1016/j.tecto.2007.09.004.
- Atwater, T., and J. Stock (1998), Pacific–North America plate tectonics of the Neogene southwest United States: An update, *Int. Geol. Rev.*, **40**, 375–402.
- Baumann, C., T. V. Gerya, and J. A. D. Connolly (2010), Numerical modelling of spontaneous slab breakoff dynamics during continental collision, *Geol. Soc. Spec. Publ.*, **332**, 99–114, doi:10.1144/SP332.7.
- Billen, M. I., and G. Hirth (2007), Rheologic controls on slab dynamics, *Geochem. Geophys. Geosyst.*, **8**, Q08012, doi:10.1029/2007GC001597.
- Burkett, E. R., and M. I. Billen (2009), Dynamics and implications of slab detachment due to ridge-trench collision, *J. Geophys. Res.*, **114**, B12402, doi:10.1029/2009JB006402.
- Dickinson, W. R. (1997), Tectonic implications of Cenozoic volcanism in coastal California, *Geol. Soc. Am. Bull.*, **109**(8), 936–954.
- Duret, T., T. V. Gerya, and D. A. May (2010), Numerical modelling of spontaneous slab breakoff and subsequent topographic response, *Tectonophysics*, doi:10.1016/j.tecto.2010.05.024, in press.
- Ferrari, L. (2004), Slab detachment control on mafic volcanic pulse and mantle heterogeneity in central Mexico, *Geology*, **32**(1), 77–80.
- Gasparon, M., G. Rosenbaum, J. Wijbrans, and P. Manetti (2009), The transition from subduction arc to slab tearing: Evidence from Capraia Island, northern Tyrrhenian Sea, *J. Geodyn.*, **47**, 30–38, doi:10.1016/j.jog.2008.06.004.
- Gerya, T. V., D. A. Yuen, and W. V. Maresch (2004), Thermomechanical modelling of slab detachment, *Earth Planet. Sci. Lett.*, **226**(1–2), 101–116.
- Grellet, C., and J. Dubois (1982), The depth of trenches as a function of the subduction rate and age of the lithosphere, *Tectonophysics*, **82**, 45–56.
- Guivel, C., et al. (2006), Miocene to late Quaternary Patagonian basalts (46–47°S): Geochronometric and geochemical evidence for slab tearing due to active spreading ridge subduction, *J. Volcanol. Geotherm. Res.*, **149**, 346–370.
- Hager, B. H. (1991), Mantle viscosity: A comparison of models from postglacial rebound and from the geoid, plate driving forces, and advected heat flux, in *NATO Advanced Research Workshop on Glacial Isostasy, Sea-Level, and Mantle Rheology, Erice, Italy, July 27–Aug. 4, 1990*, NATO ASI Ser., Ser. C, vol. 334, edited by R. Sabadini, K. Lambeck, and E. Boschi, pp. 493–513, Kluwer Acad., Dordrecht, Netherlands.
- Hall, C. E., and M. Gurnis (2005), Strength of fracture zones from their bathymetric and gravitational evolution, *J. Geophys. Res.*, **110**, B01402, doi:10.1029/2004JB003312.
- Hirth, G., and D. Kohlstedt (2003), Rheology of the upper mantle and the mantle wedge: A view from the experimentalists, in *Inside the Subduction Factory*, *Geophys. Monogr. Ser.*, vol. 138, edited by J. Eiler, pp. 83–105, AGU, Washington, D. C.
- Ismail-Zadeh, A. T., G. F. Panza, and B. M. Naimark (2000), Stress in the Descending Relic Slab beneath the Vrancea region, Romania, *Pure Appl. Geophys.*, **157**, 111–130.
- Iwamori, H. (2000), Thermal effects of ridge subduction and its implications for the origin of granitic batholith and paired metamorphic belts, *Earth Planet. Sci. Lett.*, **181**, 131–144.
- Kennett, B. L. N., and T. Furumura (2010), Tears or thinning? Subduction structures in the Pacific plate beneath the Japanese Islands, *Phys. Earth Planet. Inter.*, **180**, 52–58.
- Lister, G., B. Kennett, S. Richards, and M. Forster (2008), Boudinage of a stretching slablet implicated in earthquakes beneath the Hindu Kush, *Nat. Geosci.*, **1**, 196–201.
- Lonsdale, P. (1991), Structural patterns of the Pacific floor offshore of Peninsular California, in *The Gulf and Peninsular Province of the Californias*, edited by J. P. Dauphin and B. R. T. Simoneit, *AAPG Mem.*, **47**, 87–125.
- Mammerickx, J., and K. D. Klitgord (1982), Northern East Pacific Rise: Evolution from 25 m.y. B.P. to the present, *J. Geophys. Res.*, **87**(B8), 6751–6759.
- Manea, M., and V. C. Manea (2008), On the origin of El Chichón volcano and subduction of Tehuantepec Ridge: A geodynamical perspective, *J. Volcanol. Geotherm. Res.*, **175**, 459–471, doi:10.1016/j.jvolgeores.2008.02.028.
- Menard, H. W. (1978), Fragmentation of the Farallon plate by pivoting subduction, *J. Geol.*, **86**(1), 99–110.
- Michaud, F., et al. (2006), Oceanic-ridge subduction vs. slab break off: Plate tectonic evolution along the Baja California Sur continental margin since 15 Ma, *Geology*, **34**(1), 13–16.
- Miller, M. S., A. Gorbato, and B. L. N. Kennett (2006), Three-dimensional visualization of a new-vertical slab tear beneath the southern Mariana arc, *Geochem. Geophys. Geosyst.*, **7**, Q06012, doi:10.1029/2005GC001110.
- Moresi, L., S. Zhong, and M. Gurnis (1996), The accuracy of finite element solutions of Stokes' flow with strongly varying viscosity, *Phys. Earth Planet. Inter.*, **97**, 83–94.
- Pallares, C., et al. (2007), Slab-tearing following ridge-trench collision: Evidence from Miocene volcanism in Baja California, México, *J. Volcanol. Geotherm. Res.*, **161**, 95–117.
- Ranalli, G. (1995), *Rheology of the Earth*, 76 pp., 2nd ed., Chapman and Hall, London.
- Rosenbaum, G., M. Gasparon, F. P. Lucente, A. Peccerillo, and M. S. Miller (2008), Kinematics of slab tear faults during subduction segmentation and implications for Italian magmatism, *Tectonics*, **27**, TC2008, doi:10.1029/2007TC002143.
- Sigloch, K., N. McQuarrie, and G. Nolet (2008), Two-stage subduction history under North America inferred from multiple-frequency tomography, *Nat. Geosci.*, **1**, 458–462, doi:10.1038/ngeo231.
- Thorkelson, D. J. (1996), Subduction of diverging plates and the principles of slab window formation, *Tectonophysics*, **255**, 47–63.
- Turcotte, D. L., and G. Schubert (2002), *Geodynamics*, 2nd ed., 186 pp., Cambridge Univ. Press, Cambridge, U. K.
- van der Meulen, M. J., J. E. Meulenkaamp, and M. J. R. Wortel (1998), Lateral shifts of Appenninic foredeep depocentres reflecting detachment of subducted lithosphere, *Earth Planet. Sci. Lett.*, **154**, 203–219.
- Wessel, P., and W. F. Haxby (1990), Thermal stresses, differential subsidence and flexure at oceanic fracture zones, *J. Geophys. Res.*, **95**(B1), 375–391.
- Wortel, M. J. R., and W. Spakman (2000), Subduction and slab detachment in the Mediterranean–Carpathian region, *Science*, **290**(5498), 1910–1917.



- Yang, T., S. P. Grand, D. Wilson, M. Guzman-Speziale, J. M. Gomez-Gonzalez, T. Dominguez-Reyes, and J. Ni (2009), Seismic structure beneath the Rivera subduction zone from finite-frequency seismic tomography, *J. Geophys. Res.*, *114*, B01302, doi:10.1029/2008JB005830.
- Yogodzinski, G. M., J. M. Lees, T. G. Churikova, F. Dorendorf, G. Wöerner, and O. N. Volynets (2001), Geochemical evidence for the melting of subducting oceanic lithosphere at plate edges, *Nature*, *409*(6819), 500–504.
- Yoshioka, S., and M. J. R. Wortel (1995), Three-dimensional numerical modeling of detachment of subducted lithosphere, *J. Geophys. Res.*, *100*(B10), 20,223–20,244.
- Zhong, S. (2006), Constraints on thermochemical convection of the mantle from plume heat flux, plume excess temperature, and upper mantle temperature, *J. Geophys. Res.*, *111*, B04409, doi:10.1029/2005JB003972.
- Zlotnik, S., M. Fernández, P. Díez, and J. Vergés (2008), Modelling gravitational instabilities: Slab break-off and Rayleigh-Taylor diapirism, *Pure Appl. Geophys.*, *165*, 1491–1510, doi:10.1007/s00024-004-0386-9.
- Zoback, M. D., and J. Townend (2001), Implications of hydrostatic pore pressures and high crustal strength for the deformation of intraplate lithosphere, *Tectonophysics*, *336*, 19–30.